Green Chemistry

PAPER

View Article Online
View Journal | View Issue

Solar-driven alumina calcination for CO_2 mitigation and improved product quality†

Cite this: *Green Chem.*, 2017, **19**, 2992

Dominic Davis, ‡[a] Fabian Müller, ‡[b] Woei L. Saw, [c] Aldo Steinfeld *[b] and Graham J. Nathan *[a]

We report on the first-of-a-kind experimental demonstration of the calcination of alumina with concentrated solar thermal (CST) radiation at radiative fluxes up to 2190 suns using a 5 kW novel solar transport reactor. Aluminium hydroxide was calcined at nominal reactor temperatures over the range 1160–1550 K to yield chemical conversions of up to 95.8% for nominal residence times of approximately 3 s. Solar energy conversion efficiencies of up to 20.4% were achieved. The mean pore diameter and specific surface area of the solar-generated alumina with the greatest chemical conversion were 5.8 nm and 132.7 $m^2\ g^{-1}$, respectively, which are higher values than are typical for industrial alumina production. In addition, the product is dominated by the γ-phase, which is desirable for the downstream processing to aluminium. This suggests that CST can improve the quality of alumina over existing fossil fuel based processes though a combination of a high heating rate and avoided contamination by combustion products. Furthermore, the solar-driven process has the potential to avoid the discharge of combustion-derived CO_2 emissions for the calcination stage of the conventional Bayer process, which is typically 165 kg-CO_2 per tonne-alumina.

Received 24th February 2017,
Accepted 10th May 2017

DOI: 10.1039/c7gc00585g

rsc.li/greenchem

1 Introduction

The use of concentrated solar thermal energy (CST) for high-temperature thermal processing of minerals has the potential to reduce reliance on fossil fuels and hence also to reduce greenhouse gas (GHG) emissions.[1,2] The calcination stage of alumina refining with the Bayer process is potentially well suited to the application of CST because it is a highly endothermic process that proceeds at ~1273 K, which is readily achievable with solar tower technology. In addition, the calcination process is not sensitive to some ingress of air, which raises the possibility that direct irradiation of particles may be achievable without the need for a window to completely seal a solar reactor. However, the technical feasibility of this process is yet to be evaluated experimentally. The overall objective of this investigation is therefore to assess and demonstrate the technical feasibility of alumina calcination with direct irradiation *via* CST.

Alumina is an intermediate product in the production of aluminium and is also a product in its own right. Alumina refining accounts for approximately 27% of the primary energy used in aluminium production, over 90% of which is provided by the combustion of fossil fuels.[3] A total of 115.2 million tonnes of alumina was produced globally in 2015 at an average energy intensity of 11.9 GJ per tonne-alumina, representing a significant contribution to GHG emissions.[4] Calcination is the last step of the Bayer process, which heats the hydrated alumina (aluminium hydroxide or gibbsite, $Al(OH)_3$) from the precipitation stage, to drive off the water of hydration and form anhydrous alumina (aluminium oxide, Al_2O_3). It is an energy-intensive process, which has historically been conducted with the use of fossil fuels and a rotary-kiln.[5] However, since the oil crisis of the 1970s, with the resulting increase in the cost of fuels, stationary calciners (circulating fluidised bed, gas suspension and fluid-flash calciners) have been favoured over rotary-kilns due to their significantly reduced fuel consumption.[6,7] The process heat requirements of modern industrial calciners and estimated resulting CO_2 emissions (calculated from the combustion of methane) are now approximately 3 GJ per tonne-alumina and 165 kg-CO_2 per tonne-alumina product, respectively, for which the predominant fuel is natural gas.[8,9] Today, the increasing cost of fuels continues to be a driver for technological development of more fuel

---

[a] School of Mechanical Engineering, Centre for Energy Technology, The University of Adelaide, South Australia 5005, Australia. E-mail: graham.nathan@adelaide.edu.au
[b] Department of Mechanical and Process Engineering, ETH Zürich, 8092 Zürich, Switzerland. E-mail: aldo.steinfeld@ethz.ch
[c] School of Chemical Engineering, Centre for Energy Technology, The University of Adelaide, South Australia 5005, Australia

† Electronic supplementary information (ESI) available. See DOI: 10.1039/c7gc00585g

‡ The first two authors have contributed equally to this work.

efficient alumina calciner technology.[10] With the price of natural gas forecast to increase in some locations such as Australia,[9] and with the global need to reduce GHG emissions, there is strong incentive to seek alternative energy sources such as CST for process heat.[11] This provides the motivation for the present investigation.

The calcination of alumina is a thermal decomposition chemical reaction, which proceeds endothermically according to the following reaction:

$$2\mathrm{Al(OH)_3} \rightarrow \alpha\text{-}\mathrm{Al_2O_3} + 3\mathrm{H_2O}, \Delta\bar{h}^{\circ}_{\mathrm{calcination}} = +185.2\ \mathrm{kJ\,mol^{-1}}. \tag{1}$$

Modern plants typically process alumina (generally in the gibbsite form) within flash calciners using particles of ~100 μm in diameter transported in a gas suspension through the reactor with residence times on the order of a few seconds. A solar reactor that processes powders of similar size to a flash calciner is the solar vortex transport reactor. This employs a vortex flow to transport particles in suspension through an irradiation zone where they undergo high heating rates to drive a thermochemical reaction. Direct solar irradiation of such a suspension of reacting particles is an efficient means of heat transfer to the reactants.[12–15] Furthermore, the temperature at which alumina calcination takes place in the Bayer process, 1273–1373 K, is readily achievable in current commercially available solar tower concentrators[11] and is significantly less than the 1750 K that has been achieved previously in the solar vortex transport reactor used for solar gasification.[16] The potential for alumina to be calcined with CST has been assessed with a packed bed of boehmite (an aluminium oxyhydroxide) in a crucible positioned at the focal plane of a Fresnel concentrator by Padilla *et al.*[17] They reported 75% conversion after 10 minutes of exposure to solar radiation concentrated to 2644 suns and full conversion with exposure time of 90 minutes.[17] However to date, no assessments have been reported for the calcination of gibbsite in a practical reactor under conditions relevant to flash calcination. The industrial gibbsite calcination process shares similarities with the calcination of limestone, which takes place at ~1150 K and has previously been demonstrated with the application of CST.[18–21] This demonstration has been performed with direct irradiation in a cavity-receiver transporting a flow of entrained particles,[18] which suggests that it may also be suitable for alumina calcination. It is also noteworthy that the alumina calcination process is sensitive to the gas-phase composition, which is one reason that natural gas is a preferred fuel for alumina production.[22,23] The application of CST to the calcination process has the potential to further improve product quality by eliminating the possibility of contamination with combustion products and by reducing the significance of back-reactions from the presence of H_2O, which is a product of combustion. While these reasons suggest that the alumina calcination process is potentially well suited to solar processing, its technical feasibility cannot be determined by implication. Due to the complex, coupled nature of the process, it is necessary to assess this experimentally with a prototype solar reactor.

When gibbsite is calcined, the solid reactant evolves through various intermediate materials, including the monohydrated aluminium oxyhydroxide and several transition phases of alumina before the final, thermodynamically stable α-alumina is formed at temperatures in the range 1375–1450 K.[23,24] Both the type of intermediate transition aluminas that are formed and their relative presence in the alumina product depend particularly on the heating rate, particle size and the presence of water vapour in the reaction atmosphere.[25] Studies have previously proposed the gibbsite reaction pathways according to these parameters,[23,24,26] the consensus of which is as follows:

(a) Fine gibbsite particles (<10 μm) decompose *via* χ-Al_2O_3, an amorphous alumina, followed by κ-Al_2O_3 before reaching the final α-Al_2O_3 phase;

(b) Coarse gibbsite particles (>100 μm) decompose *via* the intermediate aluminium oxyhydroxide, boehmite (AlO(OH)). Upon further heating this progressively decomposes to γ-, δ-, and θ-Al_2O_3, before reaching the α-Al_2O_3 phase; and

(c) Gibbsite which undergoes the high heating rates of flash calcination (4700–15 000 K s^{-1}) thermally decomposes initially to the amorphous χ-Al_2O_3 as in pathway (a) before crossing over to pathway (b) and progressively forming γ-, δ-, θ-Al_2O_3, and finally the α-Al_2O_3 phase.

The formation of the intermediate species, boehmite, occurs in the range 380–575 K and is favoured by rapid heating of coarse gibbsite particles, such that there is a high local water vapour pressure within the large gibbsite particles.[23] For the case where the gibbsite particles are small enough for the water of hydration to be released without the increase of internal pressure, boehmite does not evolve.[23] Its formation is also favoured by high water vapour pressures in the transport air, as is typical of combustion gases in alumina refinery calciners.[24,27] On the basis that the use of CST will avoid the presence of H_2O as a combustion product, it can be deduced that the substitution of combustion with CST will inhibit the formation of boehmite. This would be beneficial because boehmite contains structural hydroxyls that degrade product quality for alumina smelting. The transition aluminas are characterised by their large internal porosity and resulting large surface area. They are thus useful for smelting and as catalysts. In contrast, the highly ordered and stable crystalline structure of the α-alumina phase makes it suitable for use in abrasives, refractories and ceramics.[26] The present investigation focusses on the refining of alumina for the purpose of smelting to produce primary aluminium. A study conducted by Whittington & Ilievski[24] suggests that the majority of refinery-prepared smelter grade aluminas (SGAs) reacts *via* χ-Al_2O_3 (pathway c) to feature large proportions of the γ-Al_2O_3 phase. The phase composition of numerous SGAs has previously been determined with quantitative X-ray diffraction (XRD) analysis to reveal that the product from stationary calciners comprises 60–90% γ-Al_2O_3 content while that from rotary-kiln calciners comprises 60–70% γ-Al_2O_3 content.[24] This was corroborated by

Wind & Raahauge,[28] who reported that in an industrial gas suspension calcination system only 3–8% boehmite content was found in the pre-calcination stages, and by Perander *et al.*,[29] who found that refinery-produced SGA was dominated by the γ-Al_2O_3 phase. On this basis it can be anticipated that the high heating rates inherent with solar processing will favour reaction pathway (c) to form predominantly γ-Al_2O_3. However, there is a need to assess the validity of this deduction by experiment.

The fraction of residual water in the alumina product is another important measure of product quality. This is because residual water has the propensity to drive the adverse formation of hydrogen fluoride gas during the downstream aluminium smelting process.[30] It is important that alumina is calcined to a sufficient extent for the residual water content to be in the range 0.69–0.95 wt%.[31] Alumina water content can be present in both a chemically-bound state (as in the case of aluminium hydroxides, $Al(OH)_3$ and AlO(OH)) and in a physically-adsorbed state. It has been found that both types of moisture in alumina contribute to hydrogen fluoride formation in the downstream smelting process although the physically-adsorbed moisture is more easily removed from alumina at low temperatures below 473 K, while chemically-bound moisture requires higher temperatures. The present investigation at laboratory-scale features a single pass of gibbsite particles through the solar reactor. There is thus a need to determine the maximum extent of conversion (minimum moisture content) that can be achieved with a single pass. There is also a further need to assess the partitioning of any residual water within the alumina product into these two types.

Two crucial measures of alumina product quality are its mean pore size and specific surface area (SSA). This is because, for the subsequent smelting process, the alumina serves not only as the feedstock but also as the material with which hydrogen fluoride (and other fluorine compounds) from smelter gases are removed (*via* a dry-scrubbing process).[28] The SSA and mean pore size are the primary indicators of the adsorption capacity of alumina, so that product quality is enhanced both by a larger SSA and a larger mean pore size.[32] Specifically, the subsequent process of aluminium smelting requires that the characteristic pore diameter of the alumina be an order of magnitude larger than the hydrogen fluoride molecule (having a van der Waals diameter of 0.36 nm).[32] This is to ensure high adsorption of the hydrogen fluoride in the dry-scrubbing process used in aluminium production. Previous investigations have determined that, during the calcination of gibbsite through the transition alumina, the SSA of the material increases rapidly to a maximum (>300 $m^2\ g^{-1}$) at about 673 K, due to its microporous structure (average pore size <2 nm). With higher temperatures, the extent of calcination increases, causing the average pore size to increase and the SSA to decrease and generate a mesoporous structure. Hence the final α-alumina has the lowest SSA of the various alumina phases,[6,7,23,33] and there is a trade-off between the desire to obtain both a low residual water content and a high SSA.[29,34] It has been proposed, however, that under rapid heating, such as tends to occur with flash calcination, the structural rearrangement of the gibbsite calcination sequence can be decoupled from the water removal.[33] The high heating rates possible with directly irradiated CST therefore offer the potential to produce alumina with both favourable residual moisture content and favourable microstructural properties. There is thus a need to confirm whether or not this potential benefit can be realised in practice through testing with a small scale solar reactor.

To meet these needs, the primary aim of this paper is to provide an insight into whether or not the solar-driven calcination of alumina is technically feasible. Specifically, the present investigation aims to obtain detailed understanding of the influence of key experimental parameters on the extent to which alumina may be calcined in a solar vortex transport reactor. It particularly aims to assess the influence of particle residence time and reactor temperature on the alumina product quality and to relate the performance of a laboratory-scale reactor to a full-scale device. It also aims to assess the impact of solar processing on the alumina moisture content and the alumina microstructure (mean pore size and specific surface area), which are primary measures of product quality, and to deduce the transition alumina reaction pathway.

2 Experimental methodology

2.1 Solar reactor

The solar vortex transport reactor is shown schematically in Fig. 1. This configuration was developed previously for the gasification of petroleum coke[16] and the cracking of natural gas.[35] It consists of a 200 mm-long, 100 mm-diameter ceramic lined cylindrical cavity-receiver, enclosed by a 210 mm-long, 120 mm-diameter Inconel 601 shell and a water-cooled aluminium frustum with a 3 mm-thick transparent fused quartz window. The flow of transport air and suspended $Al(OH)_3$ particles is confined to the cavity-receiver and is directly exposed to concentrated solar radiation entering through a 50 mm-diameter aperture, with an apparent absorptivity estimated to exceed 93%.[36] The window is cooled and protected from particle deposition by two injected air flows: one entering radially through a circular gap directed over the internal face of the window (with flow rate 2–4 $L_n\ min^{-1}$), and a second through four tangential nozzles on the frustum (with flow rate 1–2 $L_n\ min^{-1}$). The combination of the two purge flows suppresses the migration of particles into the frustum region. The vortex transport gas flow of synthetic air was generated by two tangentially arranged nozzles at the top (2–7 $L_n\ min^{-1}$ air flow) and the bottom (2–7 $L_n\ min^{-1}$ air flow) of the cavity and 30 mm behind the aperture. The particles were fed to the reactor through the tangential nozzle at the top of the cavity.

2.2 Reactants

Aluminium hydroxide particles in the gibbsite form with a purity of 99% were used as the reactant. Fig. 2 presents the particle size distribution of the $Al(OH)_3$, whose mean was

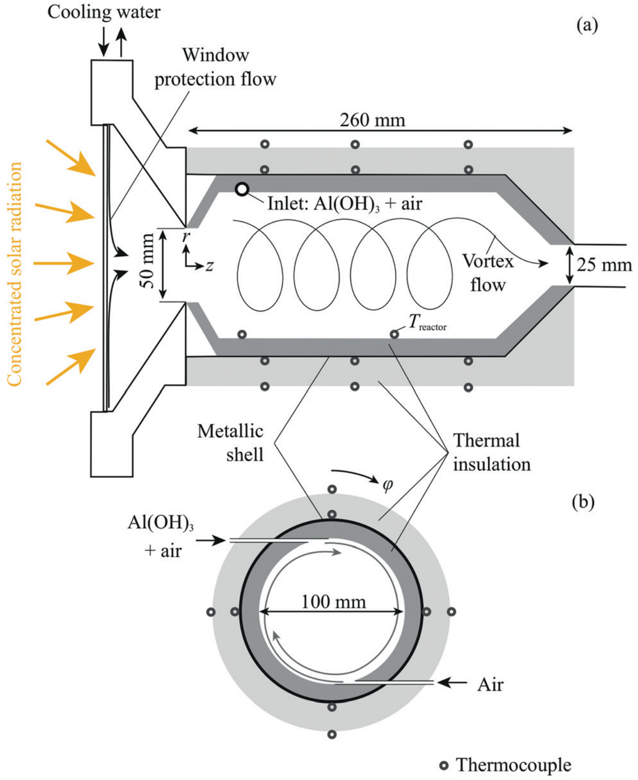

Fig. 1 Schematic diagram of (a) the axial cross section; and (b) the front view of the solar vortex transport reactor.

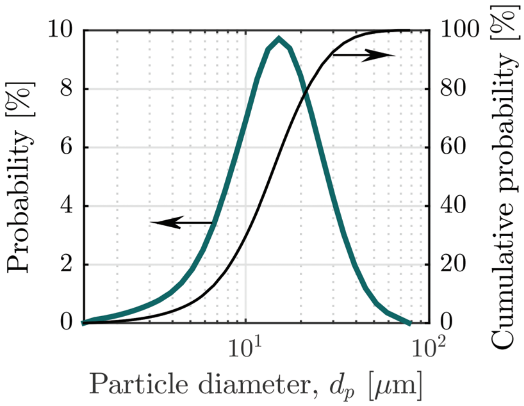

Fig. 2 Size distribution of the reactant gibbsite particles fed to the reactor.

15.5 μm as determined with laser scattering (HORIBA LA-950). The SSA of the particles was found to be 1.3 m^2 g^{-1}, determined with Brunauer–Emmett–Teller method (BET, Belsorp-max). Particles were entrained and fed using a fluidised bed feeder designed to operate over the range 1–2 g min^{-1}. Two streams of air were used to control the feeding of the Al(OH)$_3$ particles, one entering through a sintered plate at the bottom of the feeder fluidising the particles, and a second flow passing through a horizontal 5 mm-diameter carrier tube, which is aligned approximately 30 mm below the top of the static particle bed. A 1 mm hole in the upper surface of the carrier tube was used to entrain particles into the carrier tube air flow. The gibbsite mass feed rate was monitored online with weight scales (Kern FKB).

2.3 Experimental arrangement

The experimental arrangement is shown in Fig. 3. Measurements were performed with the High-Flux Solar Simulator of ETH Zurich, which comprises an array of 7 high-pressure Xenon arcs, each close-coupled with truncated ellipsoidal specular reflectors. This provides an external source of intense thermal radiation – mostly in the visible and IR spectra – that closely approximates the heat transfer characteristics of highly concentrating solar optical systems. The solar radiative input power, $\dot{Q}_s$, was measured optically with a Lambertian target and a calibrated CCD camera. $\dot{Q}_s$ was varied over the range 2.1–4.3 kW, which corresponds to mean solar concentration ratios, C, through the aperture in the range 1070–2190 suns (1 sun = 1 kW m^{-2}). Temperatures were measured with type-K thermocouples at locations shown in Fig. 1. A reference nominal reactor temperature, $T_{reactor}$, was measured with an Al$_2$O$_3$-shielded thermocouple located within the cavity as shown in Fig. 1. The nominal wall temperature, T_{wall}, was calculated as the average of seven thermocouples located on the outside of the Inconel shell (r = 61 mm),

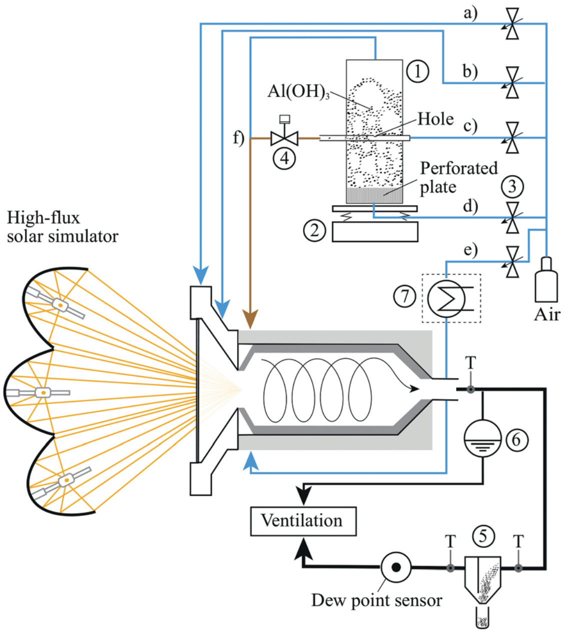

Fig. 3 Experimental arrangement used to calcine alumina with the high-flux simulated solar radiation: (T) thermocouples, (1) fluidised bed feeder, (2) weight scales, (3) mass flow controllers, (4) piston valve, (5) settling chamber (with particle collection), (6) hydrostatic over pressure system, (7) optional steam generator unit, (a) radial window purge air, (b) tangential window purge air, (c) carrier air, (d) fluidising air, (e) 2nd tangential reactor inlet (no particles), (f) fluidising air exhaust connects to other gas flows.

covered with insulation, at various z–φ locations: (50 mm, 0°); (115 mm, 0°; 90°; 180°; 270°); (190 mm, 0°; 180°). The total transport air normal flow rate, $\dot{V}_{\mathrm{air,n}}$, was controlled with electronic flow controllers (Bronkhorst HI-TEC). Dry synthetic air was used as the transport air with normal flow rates, $\dot{V}_{\mathrm{air,n}}$, in the range 12.0–20.0 $\mathrm{L_n\ min^{-1}}$. Additionally, the gibbsite particle nominal residence time, τ, within the reactor was calculated from the cavity volume, V, and the total volumetric flow rate of transport air and gas product, $\dot{V}_{\mathrm{air}}$ ($\dot{V}_{\mathrm{air,n}}$ corrected for reactor temperature). The $\dot{V}_{\mathrm{air}}$ input of the present investigation led to τ = 1.38–3.40 s. The similar value of nominal residence time in the present experimental facility to that of an industrial device despite three orders of magnitude smaller volume is attributed in part to much smaller ratio of the diameter of the inlet pipe to that of the reactor and, in part, to different methods of determining residence time. The Stokes number of the particles was calculated to be, Sk = 0.19, where:[37]

$$\mathrm{Sk} = \frac{\rho_{\mathrm{p}} {d_{\mathrm{p}}}^2 U_{\mathrm{in}}}{18 \mu D_{\mathrm{c}}}. \tag{2}$$

Since Sk ≪ 1, it is reasonable to assume that the residence time of the particles is equal to that of the gas. The $\mathrm{Al(OH)_3}$ particles were fed to the reactor with constant feeder conditions at ambient temperature and at mass flow rates, $\dot{m}_{\mathrm{Al(OH)_3}}$, in the range 0.55–2.53 $\mathrm{g\ min^{-1}}$. The particle to air volume fraction, ϕ, was controlled over the range 0.35×10^{-5}–1.66×10^{-5} with changes to either $\dot{V}_{\mathrm{air}}$ or $\dot{m}_{\mathrm{Al(OH)_3}}$, and is defined as:

$$\phi = \frac{\dot{V}_{\mathrm{Al(OH)_3}}}{\dot{V}_{\mathrm{air}}}. \tag{3}$$

The product particles were collected in a settling chamber downstream from the reactor. The water vapor concentration in the outlet air, $\dot{m}_{\mathrm{H_2O}}$, was measured online, downstream from the settling chamber, with a dew point sensor (Vaisala DMT346). Additionally, for one experimental run the water vapour partial pressure in the reactor was controlled by adding steam to the air flow of the second tangential inlet with an electric steam generator (Bronkhorst F- 201C). The steam was injected with a mass flow rate of $\dot{m}_{\mathrm{steam}}$ = 1.17 $\mathrm{g\ min^{-1}}$ corresponding to a vapour partial pressure of 68.6 mbar. Measurements were taken at approximately steady-state and isothermal (to within 26 K) conditions, which follows a period of pre-heating to the desired temperature. Operating parameters were averaged over the duration of reactant particle feeding. A summary of the operating conditions of the 19 nominally steady-state experimental runs is provided in Table 1.

2.4 Product characterisation

Representative samples were taken from the collected particles in the settling chamber for post-experimental analyses of the following parameters: the loss on ignition (LoI) determined from the relative mass change during thermogravimetric analysis (TGA, Netzsch STA 409 CD); the particle morphology imaged by scanning electron microscopy (SEM, Philips XL30); the phases present in the sample by X-ray diffraction data (XRD, Rigaku MiniFlex 600 diffractometer), and the product microstructure, which was in turn evaluated by measurement of both SSA with the Brunauer–Emmett–Teller method (BET, Belsorp-max) and pore size distribution with the Barrett–Joyner–Halenda method (BJH, Belsorp-max).

Fig. 4 presents the relative mass changes for the reactant $\mathrm{Al(OH)_3}$ and for a representative solar-processed sample collected from the settling chamber as a function of the TGA reference temperature, T_{TGA}. This shows that the $\mathrm{Al(OH)_3}$ begins to decompose at about 500 K, following which the mass loss increases to a maximum of 34.6 wt% corresponding to the complete conversion of $\mathrm{Al(OH)_3}$ to $\mathrm{Al_2O_3}$. Fig. 4 also shows that a small quantity of adsorbed moisture from the cooled, solar-processed alumina sample is released during its re-heating from ambient temperature to 423 K. The mass of this process can be quantified by the mass "Loss on Ignition" (LoI) in the

Table 1 Summary of operational conditions for the 19 nominally steady-state experimental runs

#	$\dot{Q}_{\mathrm{s}}$ [W]	$\dot{V}_{\mathrm{air,n}}$ [$\mathrm{L_n\ min^{-1}}$]	$\dot{m}_{\mathrm{steam}}$ [$\mathrm{g\ min^{-1}}$]	$\dot{m}_{\mathrm{Al(OH)_3}}$ [$\mathrm{g\ min^{-1}}$]	T_{reactor} [K]	T_{wall} [K]	ϕ [—]	τ [s]
1	2285	20.03	—	1.12	1259	1114	0.57×10^{-5}	1.74
2	2108	20.03	—	0.73	1213	1020	0.40×10^{-5}	1.91
3	3642	20.03	—	0.95	1479	1246	0.43×10^{-5}	1.56
4	2132	20.03	—	0.84	1226	934	0.51×10^{-5}	2.08
5	2316	12.03	—	1.35	1258	1122	1.13×10^{-5}	2.81
6	2117	12.03	—	1.39	1161	928	1.40×10^{-5}	3.40
7	3773	12.03	—	1.45	1454	1272	1.07×10^{-5}	2.47
8	2291	20.03	—	2.07	1230	1106	1.06×10^{-5}	1.72
9	2211	20.03	—	1.33	1216	977	0.77×10^{-5}	1.97
10	4224	20.03	—	1.98	1421	1258	0.89×10^{-5}	1.51
11	3730	12.03	—	2.32	1480	1311	1.66×10^{-5}	2.33
12	3383	17.03	—	1.26	1414	1227	0.68×10^{-5}	1.84
13	3492	12.03	—	1.75	1408	1219	1.35×10^{-5}	2.55
14	4262	19.85	—	2.53	1551	1371	1.05×10^{-5}	1.38
15	3766	16.03	—	1.06	1456	1254	0.60×10^{-5}	1.92
16	2362	16.03	—	1.14	1208	1051	0.76×10^{-5}	2.29
17	2198	16.03	—	0.55	1179	943	0.41×10^{-5}	2.58
18	3965	20.03	—	1.35	1459	1284	0.59×10^{-5}	1.50
19	3832	20.03	1.17	0.85	1439	1262	0.35×10^{-5}	1.43

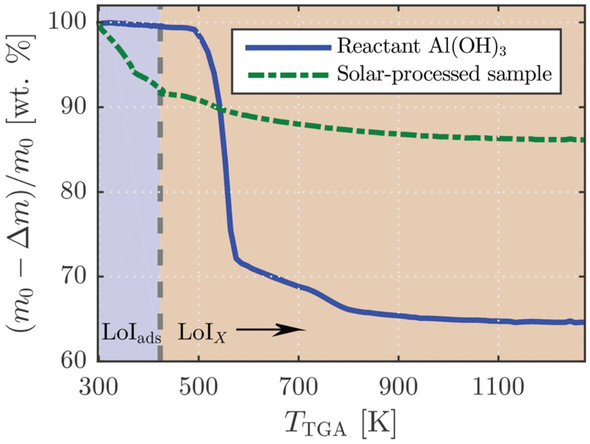

Fig. 4 Relative mass change of the reactant $Al(OH)_3$ and a representative solar-processed alumina as a function of the reference TGA temperature, T_{TGA}, during a dynamic TGA run between 298 K and 1273 K in synthetic air. The temperature ranges used in the present study for determining $\mathrm{LoI_{ads}}$ and LoI_X are indicated.

temperature range: 298–423 K, denoted here as $\mathrm{LoI_{ads}}$. The further mass loss of the solar-processed alumina from its heating to higher temperatures corresponds to the mass percentage of unreacted $Al(OH)_3$ in the solar-processed alumina. The LoI over this second range, 423–1273 K is denoted as LoI_X, and is used in the present investigation to calculate the overall molar conversion of $Al(OH)_3$ to Al_2O_3, X, according to:

$$X = \frac{2n_{\mathrm{Al_2O_3}}}{n_{\mathrm{Al(OH)_3}} + 2n_{\mathrm{Al_2O_3}}}, \tag{4}$$

where, $n_{\mathrm{Al_2O_3}}$ and $n_{\mathrm{Al(OH)_3}}$ are the molar quantities of alumina product and unreacted $Al(OH)_3$ in the solar-processed alumina (as determined from LoI_X). The ISO standard for reporting alumina moisture content is by the $\mathrm{LoI_{1273}}$, evaluated over the temperature range 573–1273 K.[30,34,38] However, it has been shown that the reactant $Al(OH)_3$ begins to decompose at temperatures below 573 K, which means that the $\mathrm{LoI_{1273}}$ underestimates the amount of unreacted $Al(OH)_3$. This provides justification for the use of $\mathrm{LoI_{ads}}$ and LoI_X in the present investigation. Errors in the TGA measurements result from the large SSA of transition aluminas and their reactivity with moisture in the air. This error affects measurement of the $\mathrm{LoI_{ads}}$ most significantly, but also affects the measurement of chemical conversion, X. The relative errors in $\mathrm{LoI_{ads}}$ and X were determined to be ±3.3% and ±18.7%, respectively, based on repetitions of TGA tests and the maximum deviation from the mean result.

3 Results & discussion

3.1 Steady-state operation

The operational conditions for the 19 nominally steady-state experimental runs listed in Table 1 resulted in T_{reactor} = 1161–1551 K and T_{wall} = 928–1371 K.§ The solar energy conversion efficiency, η, of the solar calcination process is defined to account for the energy required for the endothermic calcination process, as well as the sensible heating of the reaction products and the transport air, as follows:

$$\eta = \frac{\Delta \dot{H}}{\dot{Q}_{\mathrm{s}}} = \frac{\dot{H}^{T_{\mathrm{R}}}_{\mathrm{products}} - \dot{H}^{\circ}_{\mathrm{reactant}} + \Delta \dot{H}_{\mathrm{air}}}{\dot{Q}_{\mathrm{s}}}. \tag{5}$$

Here the sensible heat of the transport air is included in the useful energy because an industrial flash calcination process recovers the majority of such sensible heat through downstream heat exchangers, which are also used to pre-heat the particles. That is, the present solar reactor needs to both heat and react the particles, while they enter an industrial reactor hot. The performance indicators, X and η were measured to be in the range X = 84.8–95.8% and η = 8.8–20.4%, respectively. In terms of product quality parameters, the measured values of loss on ignition of adsorbed moisture were $\mathrm{LoI_{ads}}$ = 5.9–14.1%, the measured values of SSA were found to be in the range 132.7–226.6 $m^2\ g^{-1}$ and the mean pore size was measured to be in the range d_{pore} = 2.54–5.75 nm.

Fig. 5 presents the outputs from a typical experimental run (#9). Plotted are the temporal variations of $\dot{Q}_{\mathrm{s}}$, T_{reactor}, T_{wall}, $\dot{m}_{\mathrm{Al(OH)_3}}$, and $\dot{m}_{\mathrm{H_2O}}$. When the desired T_{wall} was reached and steady temperatures were measured, the particle feeding was

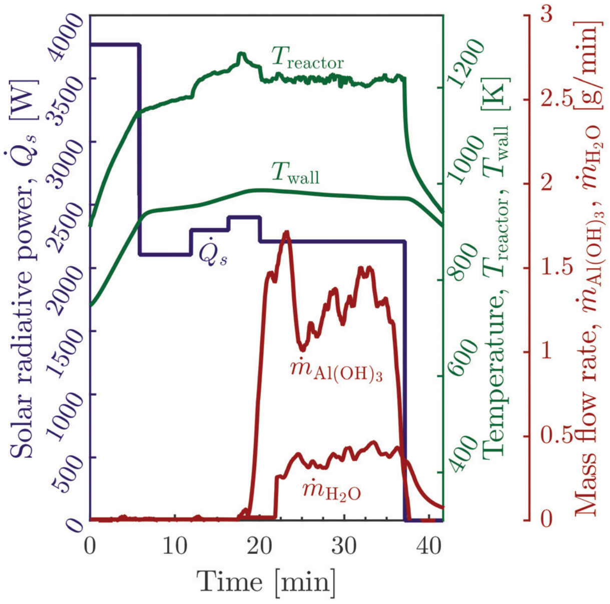

Fig. 5 Temporal variations of solar radiative power input, $\dot{Q}_{\mathrm{s}}$, reactor temperatures, T_{reactor} and T_{wall}, particle mass feed rate, $\dot{m}_{\mathrm{Al(OH)_3}}$, and mass flow rate of evolved water within the outlet stream, $\dot{m}_{\mathrm{H_2O}}$, during a representative solar experimental run (#9).

---

§ X, η and XRD results are presented as functions of T_{wall} rather than T_{reactor} due to the greater number of thermocouples contributing to the mean measurement and the lesser influence of direct irradiation on the thermocouple reading.

turned on. The period, 21–35 min, is considered to be nominally steady-state.

3.2 Extent of calcination and efficiency

Fig. 6a presents the dependence of X on T_{wall} for all experimental runs with four different values of $\dot{V}_{\mathrm{air,n}}$. It is evident that the reactor temperature has a controlling influence on the extent of conversion, so that an increase in T_{wall} results in greater X. It can also be seen that a maximum chemical conversion of 95.8% was obtained for T_{wall} = 1371 K. Despite this temperature being within the range typical of industrial flash calciners (1273–1373 K),[11] the conversion was below 100%. This can be attributed both to the much smaller scale of the reactor in the present study relative to industrial-scale calciners and to the additional stages in industrial calcination systems, incorporating both particle preheating stages and a holding vessel, which together reduce the temperature rise and/or residence time required for full conversion. Fig. 6b presents the dependence of X on τ for three T_{wall}. This shows that X is increased by an increase in τ, although the influence is relatively weak in comparison with that of T_{wall}. The trend of increasing X with longer τ is also consistent with well-established understanding of the alumina calcination reaction.[23,24] The slightly stronger influence of T_{wall} than that of τ is further evident from results of experimental run 14 with T_{wall} = 1371 K, which featured the greatest X despite having the shortest τ = 1.38 s.

Fig. 7 presents the dependence of η on $\dot{V}_{\mathrm{air}}$ (corrected for reactor temperature), for four different values of T_{wall}. A maximum energy efficiency of 20.4% was achieved for this reactor. It can be seen that η increases with a reduction in T_{wall} because both the conduction and re-radiation losses depend on the reactor wall temperature. It can also be seen that, for a given value of T_{wall}, η increases with an increase in $\dot{V}_{\mathrm{air}}$. This implies that an increase in the flow rate of air and particles causes a greater fraction of the radiation to be absorbed by the reactant and transport air than by the walls, which increases the ratio of useful heat to losses. The values of η for this reactor are low relative to industrial-scale reactors but are comparable with those from other laboratory-scale reactors.[16,20] This is because the ratio of internal surface area to internal volume of the reactor decreases with an increase in scale, causing a greater fraction of energy to be absorbed by the reactants and transport air relative to the walls of the reactor, which increases efficiency consistent with the results from Fig. 7. In addition, large scale industrial reactors are designed with heat integration and heat recovery systems to minimise heat losses and maximise efficiency.

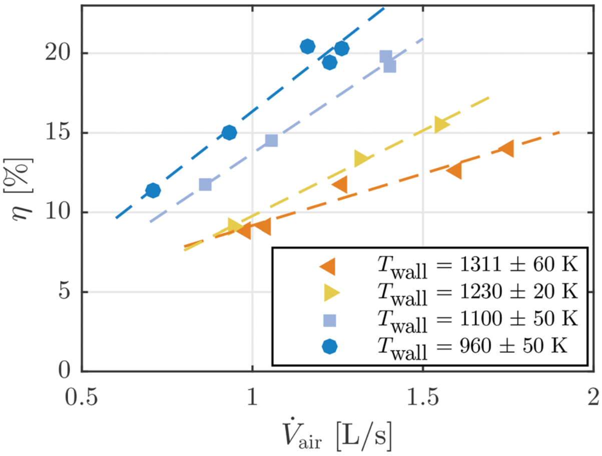

Fig. 7 The energy efficiency, η (defined in eqn (5)), of the present solar calcination reactor as a function of the volumetric flow rate of transport air, $\dot{V}_{\mathrm{air}}$, for four different wall temperatures, T_{wall}. See Table 1 for details.

3.3 Product quality: residual moisture

Fig. 8 presents the $\mathrm{LoI_{ads}}$ as a function of ϕ for four different values of T_{wall}. It can be seen that, for each value of T_{wall}, the

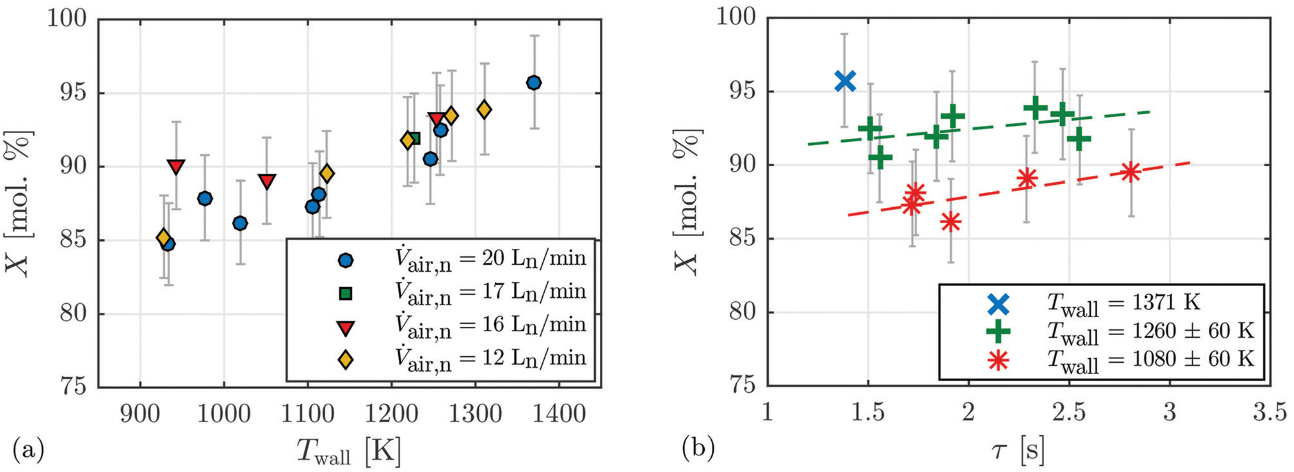

Fig. 6 The extent of chemical conversion, X, as a function of (a) the average characteristic wall temperature, T_{wall}, for four different air normal flow rates, $\dot{V}_{\mathrm{air,n}}$, and for experimental runs 1 to 17; and (b) the nominal particle residence time, τ, for three different average characteristic wall temperatures, T_{wall}. Also shown are the linear lines of best fit for the data points in the two temperature ranges.

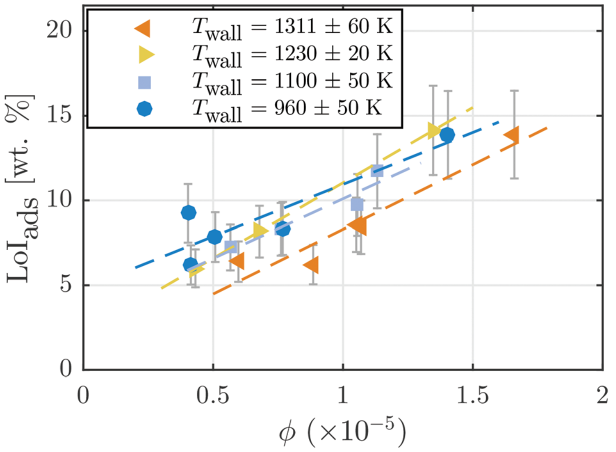

Fig. 8 Mass percentage of adsorbed moisture, LoI_{ads}, in the product from the solar reactor as a function of the particle to air volume fraction, ϕ (defined in eqn (3)), for four different wall temperatures, T_{wall}, for experimental runs 1 to 17.

Table 2 The influence of addition of steam to the transport air on the mass percentage of adsorbed moisture, LoI_{ads}, extent of chemical conversion, X, and energy efficiency, η, based on experimental runs 18 and 19

$\dot{m}_{steam}/\dot{m}_{air}$	#	LoI_{ads}	X	η
[—]		[wt%]	[mol%]	[%]
0	18	5.91	94.5	14.0
0.045	19	7.99	94.0	14.2

LoI_{ads} increases with ϕ. This can be explained by the increase in the concentration of water vapour, the gas-phase product of the reaction, due to an increase in volumetric loading of particles. That is, an increase in the partial pressure of water vapour in the reactor increases the resistance to the release of water into the gas phase. It can also be seen that T_{wall} has a second order influence on the LoI_{ads}, so that the highest T_{wall} = 1311 ± 60 K resulted in the lowest values of LoI_{ads}.

Table 2 presents the influence of the addition of steam ($\dot{m}_{steam}$ = 1.17 g min^{-1}) to the transport air flow on LoI_{ads}, X, and η, with all other operating conditions maintained nominally constant. It can be seen that the additional steam input, resulting in a water vapour partial pressure of 68.6 mbar, has a significant influence on the amount of surface moisture adsorbed by the alumina product, consistent with the trends in Fig. 8. More specifically, the LoI_{ads} was found to increase from 5.91% (run #18) to 7.99% (run #19). This can be explained by the increase in the partial pressure of water vapour in the transport air, which inhibits the diffusion of chemically-released water vapour into the gas phase. It also favours an increase in the readsorption of water vapour onto the surface of the alumina particle. For reference, the partial pressure of water vapour generated by the complete combustion of methane with 10% excess air is calculated to be 176.7 mbar, which is more than twice the 68.6 mbar used in the present experiment. Because methane is the dominant component of natural gas, which is the most common fuel used for industrial flash calciners, this implies that removing H_2O from combustion by solar calcination has the potential to provide a significant benefit to product quality by reducing the partial pressure of the gas-phase moisture. It can also be noted from Table 2, that the increase of the partial pressure of water vapour has no significant influence on X or η for the present conditions.

3.4 Product quality: alumina microstructure

Fig. 9 presents SEM micrographs of the solid alumina product from experimental runs (a) #4 (T_{wall} = 934 K), (b) #11 (T_{wall} = 1311 K), (c) #14 (T_{wall} = 1371 K), and (d) #19 (T_{wall} = 1262 K). It is clear that slit-shaped pores have formed in the particles, whose width increases with the value of T_{wall}. From previous work, this can be deduced to result from the calcination reaction mechanism, in which the structural hydroxyls (–OH) that hold gibbsite layers together are released rapidly as water during the calcination process, causing the gibbsite layers to split and form slit-shaped pores.[6,39]

Fig. 10 presents the mean pore diameter, d_{pore}, and the total specific pore volume, V_{pore}, of the solar processed alumina as a function of X. It can be seen that both d_{pore} and V_{pore} increase with an increase in X, consistent with both the SEM micrographs (Fig. 9) and the previous assessments for non-solar calcination by Perander *et al.*[6] For X = 95.8%, d_{pore} reaches up to 5.8 nm for run 14. It can also be seen from a comparison with reported mean pore sizes of typical SGAs produced with industrial flash calciners (presented as the open symbols in Fig. 10),[28,32,34] the solar process generates larger values of d_{pore} for a given value of X than does the conventional process. Extrapolation suggests that d_{pore} will continue to increase with X, so that solar-processed alumina has potential to achieve a larger mean pore size than the majority of conventionally-processed aluminas, noting the exception for two SGAs with pore size larger than 8 nm. It should also be recalled that the solar-processed alumina has been calcined with residence times in the order of a few seconds. This contrasts the industrial process, which also includes both a pre-heating stage and a holding vessel to provide additional residence time for pore growth. That is, the solar process generates a higher product quality by this measure than does the conventional processing, indicating potential to improve hydrogen fluoride adsorption capacity in the downstream dry-scrubbing process.

Fig. 11 presents the measured values of SSA for the solar-produced alumina as a function of X. The figure shows that SSA is nearly constant (mostly in the range 168–190 m^2 g^{-1}) for lower values of X in the range 85–92%, but then decreases with further increases in X to the minimum of 132.7 m^2 g^{-1} for X = 95.8%. The present values of SSA are significantly greater than previously reported values of SGA produced industrially, as shown in Fig. 11.[28] Nevertheless, more data are required before a reliable comparison with the industrial data can be made, owing to the different values of X for the experi-

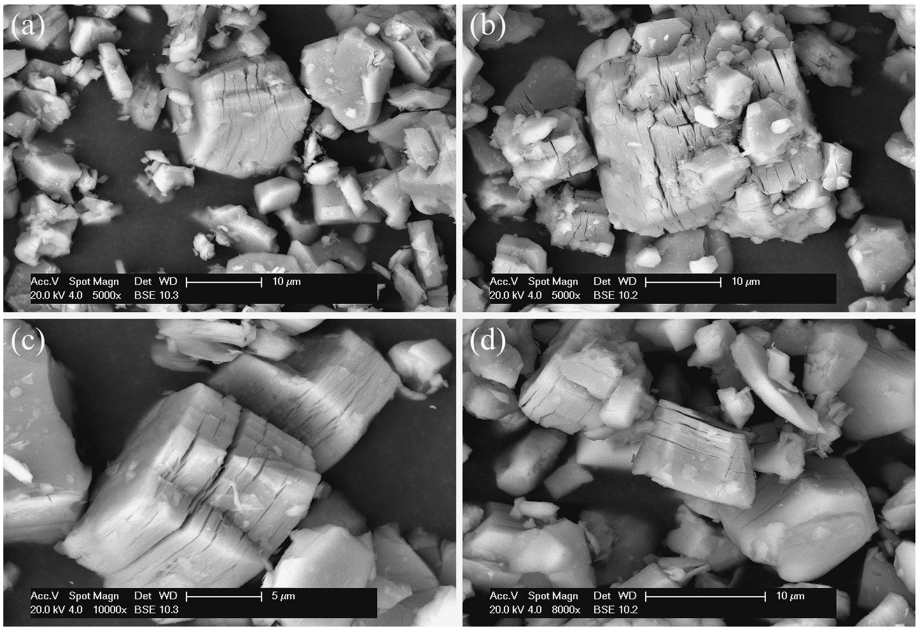

Fig. 9 SEM micrographs of solar-processed alumina obtained from experimental runs (a) #4 (T_{wall} = 934 K), (b) #11 (T_{wall} = 1311 K), (c) #14 (T_{wall} = 1371 K), and (d) #19 (T_{wall} = 1262 K) at 5000, 5000, 10 000, and 8000 magnification, respectively.

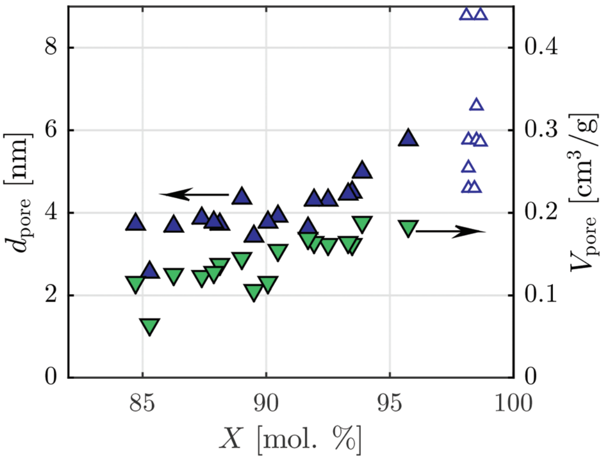

Fig. 10 Mean pore diameter, d_{pore}, and total specific pore volume, V_{pore}, of the solar-produced aluminas as a function of the extent of chemical conversion, X, for experimental runs 1 to 17. Also shown with open symbols are the typical mean pore diameter of nine SGAs produced with industrial calciners as reported in the literature.[28,32,34]

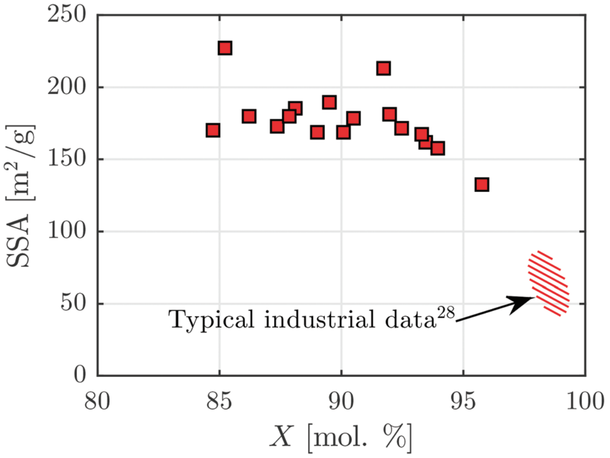

Fig. 11 Specific surface area, SSA, of the present solar-produced aluminas as a function of the extent of chemical conversion, X, for experimental runs 1 to 17. Also shown is the typical X and SSA product quality properties of SGA calcined in an industrial gas suspension calciner.[28]

mental and industrial data, which is associated with the difference in scale of the facilities.

3.5 Product quality: X-ray diffraction analysis

Fig. 12 presents a series of XRD spectra of alumina powder samples produced with different values of T_{wall}, but at constant $\dot{V}_{\mathrm{air,n}}$ = 20 $\mathrm{L_n}$ min^{-1} (ϕ = 0.40 × 10^{-5}–1.06 × 10^{-5}). For the case with T_{wall} = 934 K, the presence of unconverted reactant can be seen from the discrete diffraction peaks corresponding to gibbsite, notably from the two peaks of greatest intensity at 2θ = 18.3° and 20.3°. For higher values of T_{wall} the discrete diffraction peaks of gibbsite reduce in intensity and are replaced by the more diffuse diffraction peaks of the transition alumina. The presence of some residual gibbsite in the alumina samples, which each combine many alumina particles, indicates that a fraction of the particles did not reach sufficient temperature for long enough to convert all of the original gibbsite. Given the wide size distribution of the particles, it is likely that the residual gibbsite is preferentially partitioned in the larger particles, which require the longest residence time for

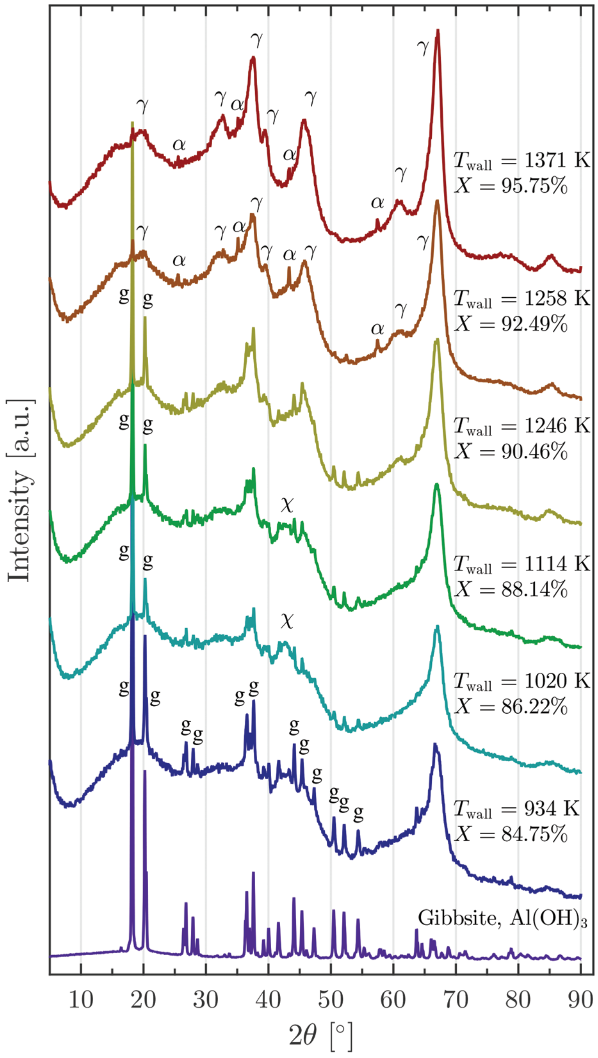

Fig. 12 X-ray diffractograms of gibbsite and solar-processed alumina samples produced with a series of reactor temperatures (experimental runs 4, 2, 1, 3, 10 and 14) with a constant normal flow rate of transport air ($\dot{V}_{\text{air,n}}$ = 20 L_n min^{-1}). The reference raw gibbsite X-ray diffractogram is also shown at 1/14th the intensity. Annotations show where the diffraction peaks correspond to reported diffraction peaks of gibbsite (g), χ-Al_2O_3, γ-Al_2O_3 and α-Al_2O_3 (COD PDF Card No. 1011081, 2015530 & 1000017).

complete conversion. However, further work will be required to verify this. For T_{wall} = 1020 K and 1114 K a broad diffuse peak at 2θ = 42.8° can be seen, which corresponds to the χ-Al_2O_3 phase.[23,24,40] For T_{wall} = 1258 K and 1371 K the χ-Al_2O_3 peak is not present and the dominant diffuse diffraction peaks occur at 2θ = 19.4°, 31.9°, 37.6°, 39.3°, 45.7°, 60.6°, and 66.7° corresponding to γ-Al_2O_3. This is corroborated by an additional analysis of the samples by Fourier Transform Infrared Spectroscopy (not shown), which found that the spectra from the solar-processed alumina samples are characterised by a broad distribution without sharp peaks. This is consistent with the alumina having a complex disordered structure, which is typical of χ-Al_2O_3 and γ-Al_2O_3.[41,42] It should also be noted that the XRD results from the two cases with the highest T_{wall} feature small discrete peaks corresponding to α-Al_2O_3 (2θ = 25.6°, 35.1°, 43.3°, and 57.5°), indicating that the particles reached the temperature at which α-Al_2O_3 forms (1375–1450 K). Although it is difficult to quantify the relative presence of the transition aluminas due to their diffuse diffraction peaks,[6,29] it is clear that γ-Al_2O_3 is the predominant phase produced during solar calcination, while small amounts of the α-Al_2O_3 phase were also observed. This is consistent with published results from refinery-produced aluminas, in which the dominant alumina phase is also γ-Al_2O_3, while α-Al_2O_3 makes up 2–9% (see Table 3).[31] Taken together, these results imply that high temperature solar calcination favours the reaction pathway of χ- to γ- to α-Al_2O_3 (pathway c[23,24,26]).

Fig. 13 presents XRD spectra of solar-processed alumina samples produced with a range of values of T_{wall} for $\dot{V}_{\text{air,n}}$ = 12 L_n min^{-1} (ϕ in the range 1.07×10^{-5}–1.66×10^{-5}). As for Fig. 12, the samples produced at lower temperatures have discrete diffraction peaks corresponding to gibbsite, which also implies the presence of unreacted gibbsite. The general trend is that the intensity of these peaks decreases with an increase in both T_{wall} and X. The exception to this is the alumina sample processed with T_{wall} = 1219 K, which exhibits gibbsite diffraction peaks with lower intensity than those of the two alumina samples processed with higher temperature. It should also be noted from Fig. 13 that the only clearly visible discrete diffraction peaks of gibbsite for the cases with low T_{wall} are those at 2θ angles of 18.3° and 20.3°. In contrast, numerous discrete gibbsite peaks are visible for the alumina samples produced with low values of T_{wall} and larger values of $\dot{V}_{\text{air,n}}$ (Fig. 12). The evolution of χ-Al_2O_3 at T_{wall} = 928 K and T_{wall} = 1122 K and the subsequent evolution of γ-Al_2O_3 is evident for both the lower and higher values $\dot{V}_{\text{air,n}}$ = 12 L_n min^{-1} and $\dot{V}_{\text{air,n}}$ = 20 L_n min^{-1}. However, diffraction peaks corresponding to the intermediate aluminium oxyhydroxide, boehmite, are also visible in the XRD traces of Fig. 13. The diffraction peaks at 2θ values of 14.5° and 28.2° also correspond to boehmite and are particularly evident from the samples calcined with T_{wall} = 1219 K and 1311 K. For the sample calcined at T_{wall} = 1311 K, the species that can be observed are unreacted gibbsite, boehmite and, most predominantly, γ-Al_2O_3. This indicates that, under these conditions, the calcination reaction follows both the χ- to γ- to α-Al_2O_3 pathway (pathway c as in Fig. 12) and the boehmite to γ- to α-Al_2O_3 pathway (pathway b[23,24,26]). The same particle size distribution was used throughout the present investigation, suggesting that the boehmite formation is attributable to the increased concentration of water vapour in the immediate presence of the reacting gibbsite particles due to the lower value of $\dot{V}_{\text{air,n}}$, which can be deduced to increase ϕ.

3.6 Projection to a 50 MW solar vortex transport reactor and comparison of the product quality with the conventional process

Table 3a presents the ratio of internal surface area to internal volume of the reactor, A_S/V, the thermal input of solar radi-

Table 3 (a) Comparison of key operational parameters of the solar vortex transport reactor (SVR) at present laboratory-scale and the equivalent values for a reactor at industrial scale, as scaled with constant inlet velocity and thermal efficiency. (b) Comparison of product quality parameters of solar-calcined alumina for the case with the highest extent of conversion (run #14), together with typical properties of Smelter Grade Alumina (SGA) produced with industrial flash calciners as reported in the literature[24,28,29,31–34]

	SVR at laboratory-scale	SVR scaled to industrial-scale
(a) Operational parameter comparison		
$\dot{Q}_s$	5 kW	50 MW
A_S/V	31.9 m^{-1}	0.319 m^{-1}
τ	1.38 s	138 s

	Solar-processed alumina (run #14)	Ref. 24, 29 and 33	Ref. 28	Ref. 31	Ref. 32	Ref. 34
(b) Product quality comparison						
LoI_{1273}	1.20 wt%		0.7–0.8 wt%	0.69–0.95 wt%	0.3–1.5 wt%	0.72–1.05 wt%
α-Al_2O_3 content	Small amounts		3–6 wt%	2–9 wt%	2–20 wt%	3.9–8.1 wt%
Gibbsite content	Small amounts		<0.1 wt%	<0.1 wt%		0.56–2.65 wt%
Dominant alumina phase	γ-Al_2O_3	γ-Al_2O_3			γ-Al_2O_3	
SSA	132.7 m^2 g^{-1}		73–81 m^2 g^{-1}	72–80 m^2 g^{-1}	68–80 m^2 g^{-1}	68.1–76.1 m^2 g^{-1}
d_{pore}	5.8 nm		6.6–8.8 nm		4.6–5.8 nm	5.7–11.2 nm

ation, $\dot{Q}_s$, and the nominal particle residence time, τ, for the case of greatest conversion in the present investigation. Predicted values for the 50 MW industrial scale are also shown, where the scale up procedure assumes constant C, constant ϕ, constant input velocity, geometric similarity and constant η (*i.e.* that $\dot{m}_{Al(OH)_3}$ scales linearly with thermal input). The resulting scale up proportionality relationships are $A_S/V \propto \dot{Q}_s^{-1/2}$ and $\tau \propto \dot{Q}_s^{1/2}$. The assumption of constant input velocity is reasonable because the minimum velocity is set by the need to transport particles, while higher values are undesirable to avoid erosion. The assumption of constant efficiency is conservative because the 100-fold reduction in A_S/V with the increase in scale will result in a significant reduction in relative heat losses.[43] Table 3a shows that, with these assumptions, the constant-velocity scale up results in a 100-fold increase in τ. Even though this represents an over-estimate of the increase in residence time because the scale-up process would also increase the relative diameter of the inlet gas stream, this is more than offset by the addition of the pre-heater and the holding vessel in the industrial process. That is, scale-up can be expected to increase X and/or reduce the value of $T_{reactor}$ relative to the present laboratory-scale investigation.

Table 3b presents the parameters used to characterise the product quality for the present alumina product with greatest X (run #14), together with typical properties of SGA produced in industrial flash calciners as reported in the literature.[24,28,29,31–34] This shows that the minimum LoI_{1273} of 1.20% achieved in the present investigation is somewhat higher than the typical value of alumina produced in industrial flash calciners. However, given that extent of conversion increases with τ, it can be deduced that the LoI_{1273} would decrease to <1% with scale up of the solar reactor, which would comply with industrial requirements.[28] Furthermore, the additional incorporation of the preheating stages and holding vessels employed in current industrial processes, which provide sufficient residence time to achieve both a high conversion and a high surface area, can be expected to allow the solar reactor to be operated at lower temperature.[28] It can also be seen that the dominant alumina phase of the present solar product is γ-Al_2O_3 with small amounts of α-Al_2O_3, which is

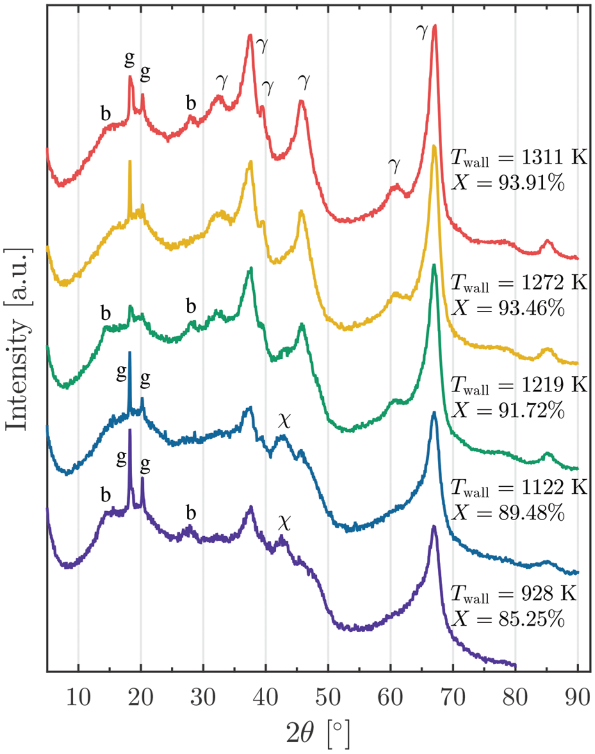

Fig. 13 X-ray diffractograms of solar-processed alumina samples produced with a series of reactor temperatures (experimental runs 6, 5, 13, 7 and 11), with a constant normal flow rate of transport air ($\dot{V}_{air,n}$ = 12 L_n min^{-1}). Annotations show where the diffraction peaks correspond to reported diffraction peaks of gibbsite (g), boehmite (b), χ-Al_2O_3 and γ-Al_2O_3 (COD PDF Card No. 1011081, 9009155 & 2015530).

consistent with that found in industrial processes. However, traces of gibbsite were also found from the XRD in the present samples of calcined solar alumina, which implies a poorer quality than is required for SGA. On the other hand, the SSA of the solar-processed alumina was found to be much higher than typical for SGA, which is consistent with the small scale, since SSA is expected to decrease with an increase in conversion. Of particular note is that the mean pore size of the solar-calcined alumina is in the upper range of industrially-produced alumina. This represents a benefit from solar calcination of alumina over conventional combustion-driven calcination.

4 Conclusions

The first-of-a-kind demonstration of the thermochemical calcination of alumina with concentrated solar thermal radiation has been undertaken with a solar vortex transport reactor. This shows that it is technically possible to calcine alumina without combustion and its concomitant CO_2 emissions, at least during those periods when the solar resource is available. The extent of chemical conversion from aluminium hydroxide to aluminium oxide was found to increase with the solar radiative power input, and hence also with the reactor temperature, to a value of up to 95.8% in this small laboratory reactor (4.3 kW of solar radiative power and an average reactor wall temperature of 1371 K). The reactor temperature was found to be the dominant experimental variable controlling the extent of solar calcination. It was also found that an increase in the nominal particle residence time has a secondary influence, also increasing the extent of conversion. Solar energy conversion efficiencies of up to 20.4% were measured for this small scale reactor, on the basis that both the sensible and chemical heat are included as the useful heat, which is consistent with the high level of heat recovery from industrial processes. A higher reactor temperature results in a drop in efficiency, due to greater re-radiation and conduction losses. It is expected, however, that the extent of calcination and energy efficiency will increase with the scale up of a solar vortex transport reactor, allowing for lower reactor temperatures due to the longer particle residence time and relatively lower heat losses associated with larger scale reactors.

Product quality assessments of the solar-calcined alumina provide strong evidence that solar calcination can result in improved quality alumina, relative to conventional industrially-calcined alumina. The addition of steam (to a water vapour partial pressure of 68.6 mbar) to the reactor transport gas flow resulted in an increase in the amount of adsorbed moisture (from 5.91% to 7.99%). This implies that the use of solar calcination, which avoids the production of steam by combustion, can reduce the amount of surface-adsorbed moisture in the alumina product (which is deleterious to alumina smelting). Consistent with this, the amount of moisture adsorbed by the alumina surface also depends on the particle to air volume fraction. This is because an increase in the partial pressure of water vapour, resulting from an increase in particle to air volume fraction, was found to inhibit diffusion of the water vapour into the transporting air phase.

The alumina microstructure analysis provided further evidence of the improved product quality from solar calcined alumina. The conditions producing a conversion of 95.8% were associated with a specific surface area of 132.7 m^2 g^{-1} and critically, a mean pore diameter of 5.8 nm. The mean pore size of the solar-produced alumina was found to increase with the extent of conversion and can be expected to increase further with scale-up. The solar-produced aluminas of the present investigation are characterised by a relatively large specific surface area and mesoporous structure (with large pore sizes), which is desirable for increased hydrogen fluoride adsorption required for the downstream dry-scrubbing process in aluminium smelting.

The X-ray diffraction analysis revealed that the alumina produced with concentrated solar thermal energy is typically characterised by a high fraction of γ-Al_2O_3 phase and a low fraction of α-Al_2O_3. This is consistent with published results from refinery-produced aluminas. Furthermore, the transition pathway was found to be consistent with that associated with high heating rates.[23,24,26] That is, the gibbsite is deduced to primarily decompose *via* the amorphous χ-alumina before reaching γ-alumina (pathway c of ref. 23, 24 and 26). Significantly, the cases with highest particle volume fraction ($\phi > 10^{-5}$), which are associated with greatest partial pressure of water vapour from the calcination reaction, were found to exhibit some decomposition of the gibbsite *via* boehmite before reaching γ-alumina and higher order transition aluminas.

Nomenclature

A_S	Reactor internal surface area [m^2]
C	Solar concentration ratio (1 sun = 1 kW m^{-2})
D_c	Reactor cavity internal diameter [m]
d_p	Mean particle diameter [μm]
d_{pore}	Mean pore diameter [nm]
$\Delta\dot{H}$	Rate of enthalpy change of a species [W]
$\Delta\bar{h}^{\circ}$	Standard enthalpy of reaction [kJ mol^{-1}]
LoI	Loss on ignition [wt%]
m	Mass of a species/sample [g]
$\dot{m}$	Mass flow rate of a species [g min^{-1}]
n	Number of moles of a species [mol]
$\dot{Q}_s$	Solar radiative power input [W]
r	Radial coordinate [mm]
Sk	Stokes number
T	Temperature [K]
U_{in}	Transport air inlet velocity [m s^{-1}]
V	Reactor internal volume [m^3]
V_{pore}	Total specific pore volume [cm^3 g^{-1}]
$\dot{V}$	Total gas volumetric flow rate
X	Chemical conversion [mol%]
z	Horizontal coordinate [mm]
η	Solar energy conversion efficiency [%]
θ	XRD incident angle [°]

μ	Dynamic viscosity [kg m^{-1} s^{-1}]
ρ	Density [kg m^{-3}]
τ	Nominal particle residence time [s]
ϕ	Particle to air volume fraction
φ	Angular coordinate [°]

Subscripts

1273	Over the temperature range 573–1273 K
ads	Of adsorbed moisture, evaluated over the range 298–423 K
air	Of air (making up the transport gas flow)
$Al(OH)_3$	Of aluminium hydroxide (gibbsite) feed particles
Al_2O_3	Of aluminium oxide (alumina) produced
calcination	Of the calcination reaction
H_2O	Of evolved water vapour
n	At normal conditions (273 K, 1 atm)
p	Of the particle
products	Of the reaction products
reactant	Of the reactant
reactor	Of the reactor cavity
steam	Of additional steam (into the transport gas flow)
TGA	Reference TGA temperature
wall	Of the reactor wall
X	Over the range for determining X, evaluated over the range 423–1273 K

Superscripts

T_R	Evaluated at reactor cavity temperature
o	Evaluated at standard conditions

Abbreviations

BET	Brunauer–Emmett–Teller
BJH	Barrett–Joyner–Halenda
CCD	Charge-coupled device
CST	Concentrated solar thermal
GHG	Greenhouse gas
ISO	International Organization for Standardization
SEM	Scanning electron microscope
SGA	Smelter grade alumina
SSA	Specific surface area
TGA	Thermogravimetric analysis
XRD	X-ray diffraction

Acknowledgements

We gratefully acknowledge the financial support by the Swiss State Secretariat for Education, Research and Innovation (Grant No. 16.0183) and the European Union's Horizon 2020 research and innovation programme (Project INSHIP – Grant No. 731287). This program has been supported by the Australian Government through the Australian Renewable Energy Agency (ARENA) program (Grant 1-USO034), and by the Australian Research Council (Grant DP150102230). The views expressed herein are not necessarily the views of the Australian Government, and the Australian Government does not accept responsibility for any information or advice contained herein. We are also grateful for the provision of an Australian Government Research Training Program Scholarship.

References

1 B. C. McLellan, G. D. Corder, D. P. Giurco and K. N. Ishihara, *J. Cleaner Prod.*, 2012, **32**, 32–44.

2 J. G. J. Olivier, G. Janssens-Maenhout, M. Muntean and J. A. H. W. Peters, *Trends in global CO_2 emissions: 2015 report*, PBL Netherlands Environmental Assessment Agency, The Hague, European Commission, Joint Research Centre, Ispra, 2015.

3 The International Aluminium Institute, Statistics, http://www.world-aluminium.org/statistics/, (accessed 4 December, 2016).

4 K. Kermeli, P.-H. ter Weer, W. Crijns-Graus and E. Worrell, *Energy Effic.*, 2015, **8**, 629–666.

5 F. Williams and H.-W. Schmidt, *Light Met.*, 2012, 135–140.

6 L. M. Perander, Z. D. Zujovic, T. F. Kemp, M. E. Smith and J. B. Metson, *JOM*, 2009, **61**, 33–39.

7 B. E. Raahauge, *Light Met.*, 2015, 73–78.

8 B. Jenkins and C. Bertrand, *IFRF Combustion J.*, 2001, 200110.

9 K. Lovegrove, S. Edwards, N. Jacobson, J. Jordan, J. Petersheim, J. Rutowitz, H. Saddler, M. Watt and J. Wyder, Renewable energy options for Australian industrial gas users, Report ITP/A0142, Australian Renewable Energy Agency, 2015.

10 C. Klett and L. Perander, *Light Met.*, 2015, 79–84.

11 T. Eglinton, J. Hinkley, A. Beath and M. Dell'Amico, *JOM*, 2013, **65**, 1710–1720.

12 D. Hirsch and A. Steinfeld, *Chem. Eng. Sci.*, 2004, **59**, 5771–5778.

13 R. Bertocchi, *Trans. ASME: J. Sol. Energy Eng.*, 2002, **124**, 230–236.

14 L. A. Dombrovsky, W. Lipiński and A. Steinfeld, *J. Quant. Spectrosc. Radiat. Transfer*, 2007, **103**, 601–610.

15 D. Mischler and A. Steinfeld, *J. Heat Transfer*, 1995, **117**, 346–354.

16 A. Z'Graggen, P. Haueter, D. Trommer, M. Romero, J. C. de Jesus and A. Steinfeld, *Int. J. Hydrogen Energy*, 2006, **31**, 797–811.

17 I. Padilla, A. Lopez-Delgado, S. Lopez-Andres, M. Alvarez, R. Galindo and A. J. Vazquez-Vaamonde, *Sci. World J.*, 2014, **2014**, 825745.

18 A. Steinfeld, A. Imhof and D. Mischler, *Trans. ASME: J. Sol. Energy Eng.*, 1992, **114**, 171–174.

19 A. Meier, E. Bonaldi, G. M. Cella, W. Lipiński and D. Wuillemin, *Sol. Energy*, 2006, **80**, 1355–1362.

20 V. Nikulshina, M. Halmann and A. Steinfeld, *Energy Fuels*, 2009, **23**, 6207–6212.

21 G. Flamant, D. Hernandez, C. Bonet and J.-P. Traverse, *Sol. Energy*, 1980, **24**, 385–395.

22 H. P. Wang, B. G. Xu, P. Smith, M. Davies, L. DeSilva and C. Wingate, *J. Phys. Chem. Solids*, 2006, **67**, 2567–2582.

23 K. Wefers and C. Misra, Oxides and hydroxides of aluminum, Report 19, Alcoa, 1987.

24 B. Whittington and D. Ilievski, *Chem. Eng. J.*, 2004, **98**, 89–97.

25 B. K. Gan, I. C. Madsen and J. G. Hockridge, *J. Appl. Crystallogr.*, 2009, **42**, 697–705.

26 V. J. Ingram-Jones, R. C. T. Slade, T. W. Davies, J. C. Southern and S. Salvador, *J. Mater. Chem.*, 1996, **6**, 73–79.

27 J. Rouquerol, F. Rouquerol and M. Ganteaume, *J. Catal.*, 1975, **36**, 99–110.

28 S. Wind and B. E. Raahauge, *Light Met.*, 2013, 155–162.

29 L. M. Perander, Z. D. Zujovic, T. Groutso, M. M. Hyland, M. E. Smith, L. A. O'Dell and J. B. Metson, *Can. J. Chem.*, 2007, **85**, 889–897.

30 C. Sommerseth, K. S. Osen, C. Rosenkilde, A. J. Meyer, L. T. Kristiansen and T. A. Aarhaug, *Light Met.*, 2012, 827–832.

31 S. Wind, C. Jensen-Holm and B. E. Raahauge, *Light Met.*, 2010, 757–764.

32 L. M. Perander, PhD thesis, The University of Auckland, 2010.

33 J. Metson, T. Groutso, M. Hyland and S. Powell, *Light Met.*, 2006, 89–93.

34 L. M. Perander, M. A. Stam, M. M. Hyland and J. B. Metson, *Light Met.*, 2011, 285–290.

35 G. Maag, G. Zanganeh and A. Steinfeld, *Int. J. Hydrogen Energy*, 2009, **34**, 7676–7685.

36 J. R. Howell, R. Siegel and M. P. Mengüç, *Thermal radiation heat transfer*, CRC press, 5th edn, 2011.

37 J. J. Derksen, S. Sundaresan and H. E. A. van den Akker, *Powder Technol.*, 2006, **163**, 59–68.

38 M. M. Hyland, A. R. Gillespie and J. B. Metson, *Light Met.*, 1997, 113–117.

39 J. de Boer, *The structure and properties of porous materials*, 1958, pp. 68–94.

40 T. Kogure, *J. Am. Ceram. Soc.*, 2004, **82**, 716–720.

41 A. Boumaza, L. Favaro, J. Ledion, G. Sattonnay, J. B. Brubach, P. Berthet, A. M. Huntz, P. Roy and R. Tetot, *J. Solid State Chem.*, 2009, **182**, 1171–1176.

42 L. Favaro, A. Boumaza, P. Roy, J. Lédion, G. Sattonnay, J. Brubach, A. Huntz and R. Tétot, *J. Solid State Chem.*, 2010, **183**, 901–908.

43 A. Z'Graggen and A. Steinfeld, *Int. J. Hydrogen Energy*, 2008, **33**, 5484–5492.